Analytical modeling and decoupling of humidity effects in nanomechanical sensing based on sorption kinetics and viscoelastic stress relaxation

Meng-Qun Feng,[1,2] Kosuke Minami,[1,3,*] Yingcheng Zhou,[1,2] and Genki Yoshikawa[1,2,†]

[1]*Research Center for Macromolecules and Biomaterials, National Institute for Materials Science (NIMS), 1-1 Namiki, Tsukuba, Ibaraki 305-0044 Japan*

[2]*Materials Science and Engineering, Graduate School of Pure and Applied Science, University of Tsukuba, 1-1-1 Tennodai, Tsukuba, Ibaraki 305-8571 Japan*

[3]*International Center for Young Scientists (ICYS), National Institute for Materials Science (NIMS), 1-1 Namiki, Tsukuba, Ibaraki 305-0044 Japan*

(Dated: April 28, 2025)

Nanomechanical sensors have gained significant attention as powerful tools for detecting target analytes; however, their signals are often influenced by environmental humidity. In static mode operation, these signals are obtained by a concentration-dependent sorption-induced mechanical strain/stress. In this study, we derive an analytical model to describe the response of viscoelastic material-coated nanomechanical sensors by incorporating humidity effects based on sorption kinetics and viscoelastic stress relaxation of receptor materials. This model is capable of reproducing the dynamic responses observed in the experimental signal responses under varying humidity conditions. Moreover, it allows for the subtraction of humidity effects, facilitating the precise isolation of analyte-specific signals. These results provide a theoretical framework for decoupling environmental background factors, such as humidity effects, in nanomechanical sensors.

I. INTRODUCTION

Nanomechanical sensors and their arrays have emerged as a powerful platform for detecting a wide range of target gases, making them particularly valuable for practical applications in artificial olfaction, including odor detection, environmental monitoring, agriculture, and healthcare and medical diagnostics [1–11]. However, humidity is a critical issue in such applications, as it significantly influences and fluctuates their performance [12–15]. Variation in humidity often leads to a baseline shift, suppression of sensor performance, and dynamic fluctuation in sensor response, complicating the accurate detection of target analytes [16–19]. For instance, Inada *et al.* [9] recently proposed statistically reproducible protocols for breath analysis to mitigate this issue by selecting features robust to the effects of humidity, yet the underlying mechanisms remain unclear. Therefore, understanding the humidity influence on sensing performance is crucial for achieving reliable detection.

In the so-called static mode operation, nanomechanical sensors are coated with a receptor material that absorbs the analyte [1, 20]. The sensing signals are obtained through the deformation induced by surface stress resulting from the sorption of target analytes, including water molecules, into the receptor material [Fig. 1(a)]. Based on theoretical models of the surface stress [21–23], such sorption behaviors in the static mode nanomechanical sensors have been extensively studied theoretically, including first-order sorption kinetics in elastic [24] and viscoelastic coatings [25–29] and two-step reaction kinetics [30]. However, these models do not cover humidity effects as a background component and an analytical investigation into the influence of humidity is essential for improving the reliability of nanomechanical sensors in practical applications.

In this study, we propose an analytical model that predicts the dynamic responses of nanomechanical sensors under varying humidity conditions. By integrating sorption kinetics and viscoelastic stress relaxation, the model provides a comprehensive description of the dynamic response during multistep injection-purge cycles. Numerical calculations based on this analytical model revealed the effects of humidity in sensor responses under different initial humidity levels and varying humidity changes. Experimental validation using a viscoelastic receptor material-coated nanomechanical Membrane-type Surface stress Sensor (MSS) [1, 31, 32] in static mode [Fig. 1(b)] under different humidity conditions demonstrates strong agreement between predicted and observed sensing responses. Furthermore, our model enables effective decoupling of the humidity effects from the sensing signals, allowing analyte-induced components in the signals to be accurately extracted in humid environments. Overcoming the long-standing challenges posed by humidity, this study establishes a robust predictive method for designing reliable nanomechanical sensor systems, advancing their practical applications in various fields.

II. THEORY

To derive the theoretical formulations, we employ a theory based on the viscoelastic behavior described by the three-parameter solid model. The model is given by [25, 26, 28, 33]

$$\sigma(t) + \tau_r \frac{\mathrm{d}\sigma}{\mathrm{d}t} = M_\infty \varepsilon(t) + \tau_r M_0 \frac{\mathrm{d}\varepsilon}{\mathrm{d}t}, \tag{1}$$

where τ_r is the time constant of stress relaxation, M_0 and M_∞ denote the unrelaxed (instantaneous) and the relaxed (asymptotic) biaxial moduli, respectively. In this model, when the coating film is significantly soft and/or thin, sorption induced

* Contact author; MINAMI.Kosuke@nims.go.jp
† Contact author; YOSHIKAWA.Genki@nims.go.jp

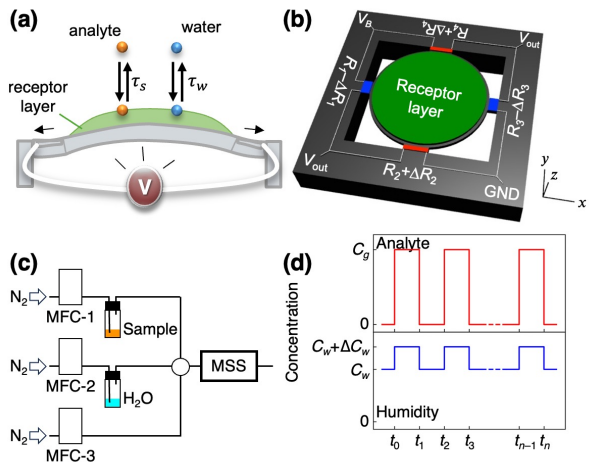

FIG. 1. Nanomechanical sensor and experimental setup. (a) Illustration of the working principle of nanomechanical MSS in static mode operation. (b) Schematic of an MSS sensing unit. (c) An experimental setup used for multistep gas injection and purge cycles under varied humidity conditions. (d) The typical rectangle injection-purge sequence, where red indicates the analyte concentration (top) and blue indicates relative humidity (bottom). The initial RH is represented as C_w.

strain (and therefore the stress) in the coating film can be approximated as uniform, thereby enabling Eq. (1) to be directly applied to cantilever-type nanomechanical sensors [26]. In the sorption-induced deformation in nanomechanical sensors, the internal strain ε_f in the coating film is modeled as a function of the concentration of analytes $C_i^g(t)$ and water $C_w^g(t)$ in the coating film as [26, 28, 29]

$$\varepsilon_f(t) = \lambda_i C_i^g(t) + \lambda_w C_w^g(t), \tag{2}$$

where λ_i and λ_w are the proportional factors corresponding to the specific volume of analyte and water divided by three for small expansion [26].

Gas sensing steps with nanomechanical sensors can be represented by a single rectangular injection or a rectangular pulse waveform, such as a multistep injection-purge sequence [28]. In this setup [Fig 1(c)], odd steps correspond to the injection process, while even steps correspond to the purge process [Fig 1(d)]. Let C_g, C_w, and ΔC_w be a constant concentration of analyte in the gas phase at the injection process (i.e., $2n$–1 steps; $n \in \mathbb{N}$), an initial constant relative humidity (RH), and constant humidity difference (i.e., humidity difference between purge and injection processes), respectively [see Fig. 1(d)]. The concentrations of analyte $C_{i,n}^g$ and water $C_{w,n}^g$ at the gas phase at the n-th step can be described as

$$C_{i,n}^g(t) = \mathbb{1}_A(n) C_g, \tag{3a}$$
$$C_{w,n}^g(t) = C_w + \mathbb{1}_A(n)\Delta C_w, \tag{3b}$$

where $\mathbb{1}_A(n)$ is the indicator function; $\mathbb{1}_A(n) = 1$ if n is odd, and zero otherwize.

In the derivation of the concentration equations of analytes within a viscoelastic receptor material coated on a nanomechanical sensor during absorption and desorption, it is assumed that the absorption of analytes follows first-order kinetics and interactions among analytes are independent, as illustrated in Fig. 1(a) [29]. Diffusion of analyte into the bulk of a coating film is generally a rate-limiting process in absorption. Under Fickian diffusion, the absorption rate becomes proportional to the difference between the equilibrium concentration in the coating film and the concentration of analytes absorbed in the film. From Eq. (3), the reaction rate of the concentration of analyte $C_{i,n}$ and water $C_{w,n}$ in the receptor material at the n-th step can be modeled as

$$\frac{dC_{i,n}}{dt} = \frac{1}{\tau_s}\left[K_p C_{i,n}^g(t) - C_{i,n}(t)\right], \tag{4a}$$
$$\frac{dC_{w,n}}{dt} = \frac{1}{\tau_w}\left[K_w C_{w,n}^g(t) - C_{w,n}(t)\right], \tag{4b}$$

where τ_s and τ_w denote the diffusion time constants of analyte and water, respectively; K_p and K_w are the partition coefficients of analyte and water, respectively [28, 29]. Although Eq. (3) is a step function, the dynamic concentration must be a continuous function. As for the boundary conditions at $t = t_n$, $C_{w,n}(t_n) = C_{w,n+1}(t_n)$ and at the beginning of the first injection ($t = t_0$), the concentration should be $C_{w,n=1}(t_0) = K_w C_w$. By solving differential equations in Eq. (4b) with Eq. (3b), the recurrence relation between the $2m$-th and $2(m$+1)-th purge processes and that between $(2m$+1)-th injection and $2m$-th purge processes for water can be found as

$$C_{w,2m+1}(t) - C_{w,2m}(t) = K_w \Delta C_w \left(1 - e^{-\frac{t-t_{2m}}{\tau_w}}\right), \tag{5a}$$
$$C_{w,2(m+1)}(t) - C_{w,2m}(t) = K_w \Delta C_w \left(e^{-\frac{t-t_{2m+1}}{\tau_w}} - e^{-\frac{t-t_{2m}}{\tau_w}}\right), \tag{5b}$$

with the concentrations at the first injection and purge processes given by

$$C_{w,n=1}(t) = K_w \left[C_w + \Delta C_w \left(1 - e^{-\frac{t-t_0}{\tau_w}}\right)\right], \tag{6a}$$
$$C_{w,n=2}(t) = K_w \left[C_w + \Delta C_w \left(e^{-\frac{t-t_1}{\tau_w}} - e^{-\frac{t-t_0}{\tau_r}}\right)\right]. \tag{6b}$$

For analyte, see [28]. Then, the recurrence relations in Eq. (5) with Eq. (6) can be solved to obtain the concentrations of water in the receptor material at the $(2m$–1)-th and $2m$-th steps as well as the concentrations of analyte [28, 29], and hence the dynamic concentration $C_{i,n}$ and $C_{w,n}$ at any time t of the n-th step can be simplified as

$$C_{i,n}(t) = K_p C_g \left(\mathbb{1}_A - a_{s,n}\right), \tag{7a}$$
$$C_{w,n}(t) = K_w \left[C_w + \Delta C_w \left(\mathbb{1}_A - a_{w,n}\right)\right], \tag{7b}$$

with

$$a_{s,n}(t) = \sum_{j=0}^{n-1} (-1)^j e^{-\frac{t-t_j}{\tau_s}}, \quad a_{w,n}(t) = \sum_{j=0}^{n-1} (-1)^j e^{-\frac{t-t_j}{\tau_w}}. \tag{8}$$

The substitution of Eqs. (2) and (7) into Eq. (1) yields the differential equation of the dynamic stress change in a viscoelastic receptor of nanomechanical sensors at the n-th step

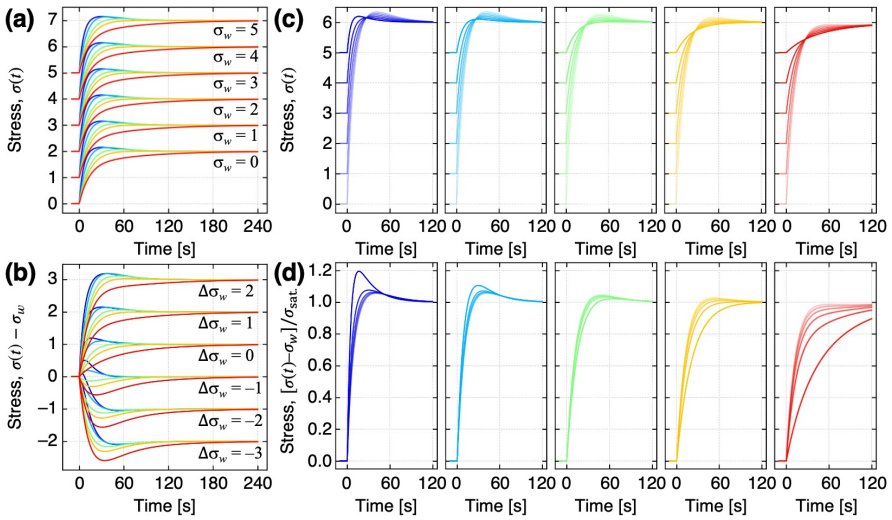

FIG. 2. Numerical calculations of the signal responses for multistep injection-purge cycles using the derived model in Eq. (9). (a) Responses to analytes with different τ_s with the fixed humidity difference ($\Delta\sigma_w = 1$) under varied initial humidity. (b) Offset responses $\sigma(t) - \sigma_w$ to analytes with different τ_s with varied humidity differences $\Delta\sigma_w$. (c,d) Model responses to highly humidified analytes, i.e., fixed ($\sigma_w + \Delta\sigma_w = 5$) under varied initial humidity σ_w. Responses $\sigma(t)$ (c) and normalized responses $[\sigma(t) - \sigma_w]/\sigma_{\text{sat.}}$ (d) are shown. Colors indicate the different τ_s: blue, τ_s = 5 [s]; sky blue, τ_s = 10 [s]; green, τ_s = 20 [s]; yellow, τ_s = 30 [s]; red, τ_s = 60 [s]. Other parameters are fixed: $\sigma_i = 1$; τ_w = 15 [s]; M_0/M_∞ = 0.72/0.51; τ_r = 22 [s].

$\sigma_n(t)$. In the case of the diffusion time constants do not equal to the relaxation time constant, i.e., $\tau_s \neq \tau_r$ and $\tau_w \neq \tau_r$, the differential equation can be solved and found the recurrence relation between the $2m$-th and $2(m+1)$-th purge processes and that between $(2m+1)$-th injection and $2m$-th purge processes with the stresses at the first injection and purge processes [Appendix A]. The recurrence relations in Eq. (A1) with Eq. (A2) can be solved to obtain the dynamic stress change at the $(2m-1)$-th and $2m$-th steps, and hence the dynamic stress change $\sigma_n(t)$ at any time t of the n-th step can be simplified as

$$\begin{aligned}\sigma_n(t) =& \sigma_i\left[\mathbb{1}_A - \alpha_i a_{s,n} - (1-\alpha_i)a_{r,n}\right] + \sigma_w \\ &+ \Delta\sigma_w\left[\mathbb{1}_A - \alpha_w a_{w,n} - (1-\alpha_w)a_{r,n}\right],\end{aligned} \tag{9}$$

with stress components in sorption kinetics $a_{s,n}$ and $a_{w,n}$ in Eq. (8) and in viscoelastic stress relaxation $a_{r,n}$ at any time t of the n-th step, which is given by

$$a_{r,n}(t) = \sum_{j=0}^{n-1} (-1)^j e^{-\frac{t-t_j}{\tau_r}}, \tag{10}$$

where $\sigma_i = M_\infty \lambda_i K_p C_g$, $\sigma_w = M_\infty \lambda_w K_w C_w$, and $\Delta\sigma_w = M_\infty \lambda_w K_w \Delta C_w$; and α_i and α_w are respectively

$$\alpha_i = \frac{1}{\tau_s}\left(\frac{M_0}{M_\infty} - \frac{\tau_s}{\tau_r}\right)\left(\frac{1}{\tau_s} - \frac{1}{\tau_r}\right)^{-1}, \tag{11a}$$

$$\alpha_w = \frac{1}{\tau_w}\left(\frac{M_0}{M_\infty} - \frac{\tau_w}{\tau_r}\right)\left(\frac{1}{\tau_w} - \frac{1}{\tau_r}\right)^{-1}, \tag{11b}$$

if $\tau_s \neq \tau_r$ and $\tau_w \neq \tau_r$.

If the relaxation time constant equals one of the diffusion time constant (i.e., $\tau_s = \tau_r$ or $\tau_w = \tau_r$), the recurrence relations between the $2m$-th and $2(m+1)$-th purge processes and that between $(2m+1)$-th injection and $2m$-th purge processes can be found similarly by substituting Eqs. (2) and (7) into Eq. (1) with the stresses at the first injection and purge processes [Appendix A]. The recurrence relations in Eq. (A3) with Eq. (A4) if $\tau_s = \tau_r$ and in Eq. (A5) with Eq. (A6) if $\tau_s \neq \tau_r = \tau_w$ can be solved to obtain the dynamic stress change at the $(2m-1)$-th and $2m$-th steps. Then, the dynamic stress change $\sigma_n(t)$ in the cases of $\tau_s = \tau_r \neq \tau_w$ and $\tau_s \neq \tau_r = \tau_w$ respectively can be simplified as

$$\begin{aligned}\sigma_n(t) =& \sigma_i\left[\mathbb{1}_A - a_{r,n} + \beta_r b_{r,n}\right] + \sigma_w \\ &+ \Delta\sigma_w\left[\mathbb{1}_A - \alpha_w a_{w,n} - (1-\alpha_w)a_{r,n}\right],\end{aligned} \tag{12a}$$

$$\begin{aligned}\sigma_n(t) =& \sigma_i\left[\mathbb{1}_A - \alpha_i a_{s,n} - (1-\alpha_i)a_{r,n}\right] + \sigma_w \\ &+ \Delta\sigma_w\left[\mathbb{1}_A - a_{r,n} + \beta_r b_{r,n}\right],\end{aligned} \tag{12b}$$

where

$$\beta_r = \frac{1}{\tau_r}\left(\frac{M_0}{M_\infty} - 1\right), \tag{13}$$

$$b_{r,n} = \sum_{j=0}^{n-1} (-1)^j (t - t_j) e^{-\frac{t-t_j}{\tau_r}}. \tag{14}$$

The stress $\sigma_n(t)$ given in Eqs. (9) and (12) is directly proportional to the signal responses of nanomechanical sensors [26, 28]. It should be noted that the amplitude (intensity) $\sigma_{\text{sat.}}$ at the equilibrium or steady state of the injection process can be described as

$$\sigma_{\text{sat.}} = \left[\lim_{t\to\infty} \sigma_n(t)\right] - \sigma_n(t_0) = \sigma_i + \Delta\sigma_w, \tag{15}$$

where $\sigma_n(t_0) = \sigma_w$. The stress σ_w derived from initial humidity C_w only influences the baseline.

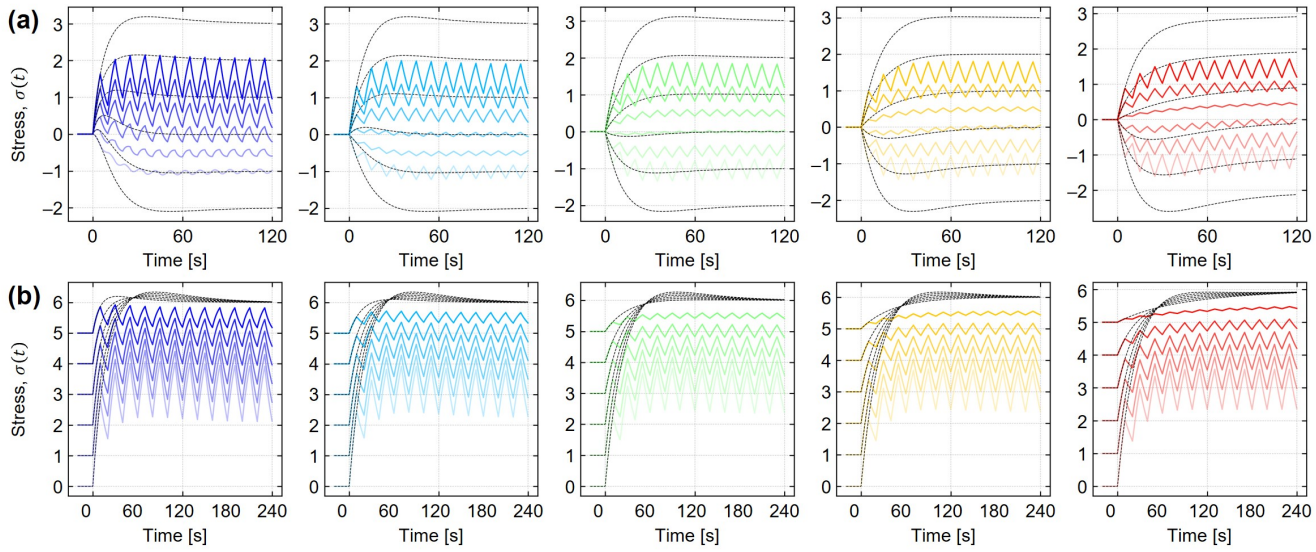

FIG. 3. Numerical calculations of the signal responses for multistep injection-purge cycles using the derived model in Eq. (9). (a) Offset response $\sigma(t) - \sigma_w$ to analytes with different τ_s with varied humidity differences $\Delta\sigma_w$. (b) Model responses to highly humidified analytes, i.e., fixed ($\sigma_w + \Delta\sigma_w = 5$) under varied initial humidity σ_w. Colors indicate the different τ_s: blue, τ_s = 5 [s]; sky blue, τ_s = 10 [s]; green, τ_s = 20 [s]; yellow, τ_s = 30 [s]; red, τ_s = 60 [s]. Other parameters are fixed: σ_i = 1; τ_w = 15 [s]; M_0/M_∞ = 0.72/0.51; τ_r = 22 [s]; $T = t_n - t_{n-1}$ = 10 [s], where T is the duration.

III. NUMERICAL CALCULATIONS

The nanomechanical sensing responses were numerically calculated under the influence of humidity using the derived equation in Eq. (9), as illustrated in Fig. 2. In our previous study, we demonstrated that the diffusion time constants τ_s can be robustly extracted even under varying relative humidity conditions [11]. Therefore, we first numerically calculated the influence of the initial humidity C_w. Figure 2(a) shows the stress $\sigma_n(t)$ with a fixed humidity difference, $\Delta C_w \propto \Delta\sigma_w = 1$, under varied initial humidity, $C_w \propto \sigma_w$. Since the sorption behaviors of analyte and water are assumed to be independent in this study, as expected, increasing the initial humidity C_w only increases the baseline, i.e., σ_w in Eq. (9), upward while maintaining their dynamic behavior. In contrast, the humidity change ΔC_w—the humidity difference between purge and injection processes—greatly influences the dynamic responses of nanomechanical sensors as can be seen in Fig. 2(b) and Fig. S1 in the Supplemental Material [34].

It should be noted that the present model in Eq. (9) also allows numerical calculations in the cases of negative humidity differences ($\Delta\sigma_w < 0$), such as when the humidity of target gas is lower than that of the purge gas. In these cases, not only the undershoot trends (i.e., the desorption of water molecules) but also the overshoot trends are calculated. For example, in the case of τ_s = 5 [s] and τ_w = 15 [s] with $\Delta\sigma_w$ = –1 or –2 in Fig. 2(b) and Fig. S1 in the Supplemental Material [34], the overshoot trends are observed, originating from the rapid absorption of analytes, and subsequently, the response drops due to the slower desorption of water as well as viscoelastic stress relaxation.

The present model in Eq. (9) is also applicable to the multistep injection-purge cycles, i.e., rectangular pulse-wave like injection purge cycles [Fig. 1(d)] [28]. Figure 3(a) shows the numerically calculated responses to the various humidity changes, including negative humidity difference, $\Delta\sigma_w < 0$ (see also Fig. S2 in the Supplemental Material [34]). Overall trends, including baseline drifts for the multistep injection-purge cycles, align with the trends observed in single injection curves, as shown by dashed lines in Fig. 3(a). These characteristic baseline transitions clearly indicate the viscoelastic response by sorption-induced nanomechanical sensing.

More importantly, the present model is capable of numerically calculating responses to fixed humidity in a target sample, particularly, for highly humidified samples such as beverages and exhaled breath [2, 5–10]. In practical applications of olfactory sensors, e.g., in breath diagnosis [7–10], the exhaled breath typically contains almost 100%RH, while the ambient air used as purge gas depends on the surrounding relative humidity. In our previous study towards breath diagnosis, measurements of exhaled breath samples with the well-controlled humidity in purge gas yield high reproducibility, while the normalization of the signal can reduce the humidity influence if appropriate features are selected [9]. Figures 2(c) and 2(d) show the numerically calculated signal responses of the model for a highly humidified sample, where the total humidity is fixed, i.e., resulting stress $\sigma_w + \Delta\sigma_w = 5$, while the initial humidity varies σ_w ranging from 0 to 5. When the total humidity in the sample is fixed, the humidity difference ΔC_w depends on the initial humidity, resulting in a change in the dynamic response σ, even when the concentration of analyte C_g remains fixed, as shown in Fig. 2(c). Since $\lim_{t\to\infty}\sigma(t) = \sigma_i + \sigma_w + \Delta\sigma_w$, the stress at equilibrium state is the same as shown in Fig. 2(c). The initial humidity has a

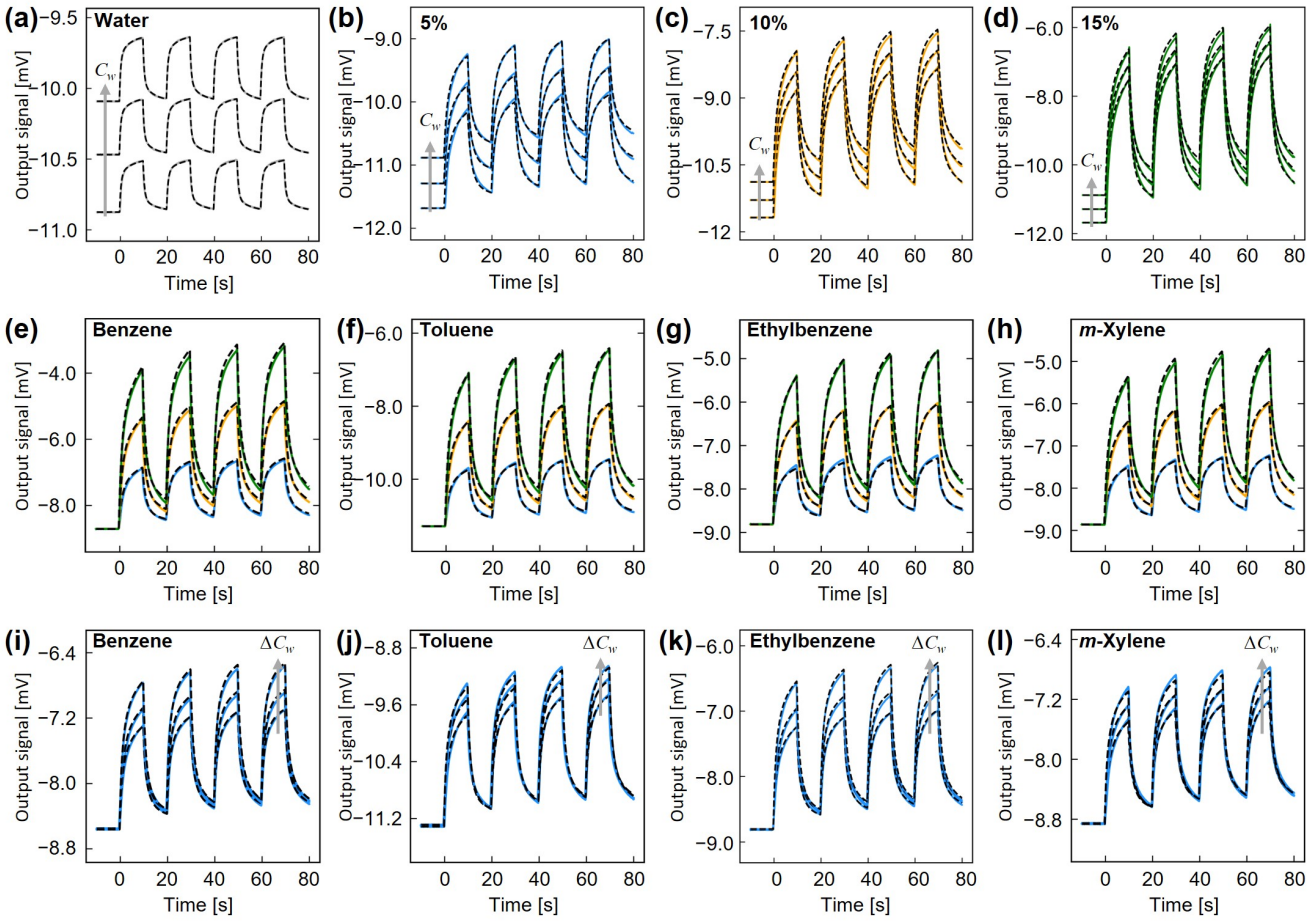

FIG. 4. Prediction of dynamic responses to humidity environments measured by polymer-coated MSS. (a) Responses to pure water with different initial humidity at C_w = 0%RH, 20%RH, and 40%RH. (b–d) Responses to a fixed humidity change of ΔC_w = 20%RH with toluene concentration C_g of 5% (b), 10% (c), and 15% (d) under varied initial humidity conditions at C_w = 0%RH, 20%RH, and 40%RH. (e–h) Responses to BETX at different concentrations under ΔC_w = 20%RH: benzene (e), toluene (f), ethylbenzene (g), and *m*-xylene (h). Initial humidity is fixed at C_w = 20%RH. Colors indicate the analyte concentrations C_g: blue, 5%; orange, 10%; and green, 15%. (i–l) Responses to BETX at concentration C_g = 10% under varied humidity differences ΔC_w: benzene (i), toluene (j), ethylbenzene (k), and *m*-xylene (l). Initial humidity is fixed at C_w = 20%RH. Humidity differences ΔC_w are 20%RH, 30%RH, and 40%RH. Dashed lines indicate the predicted responses based on the extracted fitting parameters using Eq. (9).

greater influence on the responses of the multistep injection-purge cycles for the highly humidified model in Fig. 3(b) and Fig. S3 in the Supplemental Material [34]. Figure 2(d) shows the normalized offset responses, $[\sigma(t) - \sigma_w]/\sigma_{\mathrm{sat.}}$, for the highly humidified model. The initial humidity influences the part of the dynamic responses σ depending on the time t. These results support the influence of humidity on breath analysis [9].

IV. EXPERIMENTS

Polycaprolactone (PCL) was purchased from Sigma-Aldrich and employed as a receptor material for MSS (Schematic of the MSS structure is shown in [Fig. 1(b)]. *N,N*-Dimethylformamide (DMF; 99.5%; Wako Pure Chemical Industries, Ltd.) was used as the solvent for preparing receptor material solutions. For sensing measurements, toluene (99.8%; Sigma-Aldrich), benzene (>99.5%; Kanto Chemical Co., Inc.), ethylbenzene (99.8%; Sigma-Aldrich), *m*-xylene (>98.0%; Kanto Chemical Co., Inc), and ultrapure water (MilliQ, Merck MilliPore) were used as target sample gases. All chemicals and materials were used as received.

To prepare PCL-coated MSS, PCL was dissolved in DMF at a concentration of 1.0 g/L. The resulting solution was deposited onto the surface of an MSS chip using an inkjet spotter (LaboJet-600 Bio, MICROJET Corporation) equipped with a nozzle (IJHBS-300, MICROJET Corporation). To accelerate the evaporation of DMF, the inkjet stage was maintained at 80 °C during the deposition process. For inkjet spotting, 300 shots, delivering approximately 300 pL per shot, were applied to each membrane. The resulting MSS chip was subsequently employed in sensing measurements.

The MSS chip was mounted in a custom-made Teflon-

TABLE I. Extracted fitting parameters of pure water at different concentrations.

ΔC_w [%RH]	C_w [%RH]	$\gamma\Delta\sigma_w$ [a] [mV]	τ_w [a] [s]	τ_r [a] [s]	M_0/M_∞ [a]
20	0	0.392 ± 0.002	6.596 ± 0.193	0.608 ± 0.004	7.833 ± 0.161
	20	0.402 ± 0.002	4.805 ± 0.028	0.518 ± 0.004	6.764 ± 0.005
	40	0.433 ± 0.004	4.582 ± 0.260	0.536 ± 0.006	6.280 ± 0.271
30	0	0.600 ± 0.003	5.889 ± 0.109	0.561 ± 0.002	7.552 ± 0.114
	20	0.633 ± 0.003	4.671 ± 0.068	0.527 ± 0.002	6.478 ± 0.068
	40	0.706 ± 0.003	4.654 ± 0.069	0.547 ± 0.005	6.241 ± 0.055
40	0	0.797 ± 0.001	5.250 ± 0.035	0.545 ± 0.003	6.973 ± 0.067
	20	0.840 ± 0.009	4.343 ± 0.044	0.525 ± 0.001	6.076 ± 0.049
	40	0.926 ± 0.004	4.335 ± 0.063	0.550 ± 0.003	5.820 ± 0.054

[a] An average value ± standard deviation from six independent measurements

TABLE II. Extracted fitting parameters of pure BTEX at different concentrations.

Sample	C_g [a] [%]	$\gamma\sigma_i$ [a] [mV]	τ_s [a] [s]	τ_r [a] [s]	M_0/M_∞ [a]
Benzene	5	2.235 ± 0.017	22.410 ± 1.052	1.614 ± 0.036	6.901 ± 0.149
	10	4.380 ± 0.014	18.265 ± 0.189	1.364 ± 0.015	6.612 ± 0.019
	15	6.595 ± 0.032	18.088 ± 0.419	1.303 ± 0.010	6.813 ± 0.097
Toluene	5	1.918 ± 0.012	29.587 ± 2.120	1.804 ± 0.020	7.708 ± 0.304
	10	3.835 ± 0.018	23.000 ± 1.252	1.609 ± 0.032	6.956 ± 0.185
	15	5.723 ± 0.011	20.155 ± 0.429	1.457 ± 0.017	6.722 ± 0.056
Ethylbenzene	5	1.562 ± 0.012	34.099 ± 3.443	1.902 ± 0.025	8.044 ± 0.473
	10	3.136 ± 0.004	25.011 ± 1.361	1.731 ± 0.039	6.842 ± 0.197
	15	4.709 ± 0.017	22.240 ± 0.734	1.602 ± 0.021	6.537 ± 0.116
m-Xylene	5	1.679 ± 0.004	30.862 ± 0.971	1.919 ± 0.011	7.086 ± 0.126
	10	3.337 ± 0.011	24.460 ± 0.516	1.741 ± 0.011	6.397 ± 0.065
	15	4.977 ± 0.016	22.292 ± 0.374	1.622 ± 0.010	6.250 ± 0.050

[a] An average value ± standard deviation from six independent measurements

based chamber placed inside an incubator maintained at 25.00 ± 0.02 °C. The chamber was connected to a gas control system with three mass flow controllers (MFCs), two vials containing the target liquid sample and water, and a mixing chamber [Fig. 1(c)]. Two MFCs (MFC-1 and MFC-2) were used to deliver vapors from the vials to the chamber. During the vapor injection process, humidified samples with varying concentrations were generated by adjusting the flow rates of the MFCs. The target analyte flow rate was controlled between 0 and 15 mL/min, while the humidity flow rate ranged from 0 to 80 mL/min. MFC-3 was employed to dilute the vapor mixture and purge the chamber. The vapor injection and purge were switched at every 10 s [Fig. 1(d)]. The total gas flow rate was kept constant at 100 mL/min throughout the experiments. This setup allowed the analyte concentration ratio (P_i/P_0) to be varied between 0% and 15%, where P_i and P_0 represent the partial pressure and saturated vapor pressure of the analyte, and the relative humidity to be adjusted from 0%RH to 80%RH. Nitrogen gas was used as both the carrier and the purging gases. The measurements were conducted with a bridge voltage of –0.5 V, and data were recorded at a sampling frequency of 20 Hz. The data acquisition program, designed and developed in LabVIEW (Emerson Electric Co.), was implemented for collecting, processing, and real-time visualization of sensor responses.

The fitting parameters for pure vapors were extracted using the least squares method with a trust region reflective algorithm implemented in Python 3 with the SciPy module, as described in prior work [28]. The optimized parameters in this process included the amplitude constants ($\gamma\sigma_i$ and $\gamma\Delta\sigma_w$), diffusion time constant (τ_s), relaxation time constant (τ_r), the ratio of unrelaxed to relaxed biaxial moduli (M_0/M_∞), and the initial injection time (t_0). These parameters were estimated using the formula shown in Eq. (9) (see Sec. II). Initial guesses for these parameters were set as follows: $\gamma\sigma_i = \max(V_{\text{out}}) - \min(V_{\text{out}})$, $M_0/M_\infty = 5$, $\tau_s = 50$ [s], $\tau_r = 6$ [s], and $t_0 = 0$ [s], where γ is the proportionality factor (see Sec. II) and V_{out} represents the signal responses. Lower and upper bounds applied to these parameters were: for analyte, $\gamma\sigma_i > 0$ [mV], $M_0/M_\infty \geq 1$, $\tau_w > 0$ [s], $\tau_r > 0$ [s], and $-1 < t_0 < 2$ [s]; for water, $\gamma\Delta\sigma_w > 0$ [mV] with increasing humidity or $\gamma\Delta\sigma_w < 0$ [mV] with decreasing humidity, $M_0/M_\infty \geq 1$, $\tau_w > 0$ [s], $\tau_r > 0$ [s], and $-1 < t_0 < 2$ [s].

V. EXPERIMENTAL VALIDATIONS

The validation of the proposed model, as described in Eq. (9), was achieved through experimentally measured signal responses from viscoelastic material-coated MSS [1, 31, 32] exposed to humified target analytes. The target analytes in this study are BTEX (benzene, toluene, ethylbenzene, and

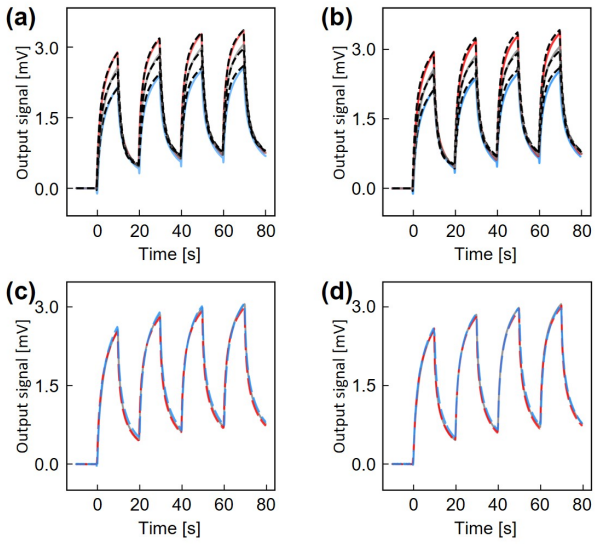

FIG. 5. Responses to toluene under positive and negative humidity changes ($\Delta C_w = \pm 20\%$RH). (a,b) The responses to toluene vapor at $C_g = 10\%$ under positive (red; $\Delta C_w = 20\%$RH) and negative humidity changes (blue; $\Delta C_w = -20\%$RH). The initial humidity conditions are $C_w = 20\%$RH (a) and $C_w = 40\%$RH (b). The output signals to pure toluene (i.e., $C_w = \Delta C_w = 0\%$RH) are also shown as gray lines. Dashed lines are the predicted responses based on the extracted fitting parameters, respectively. (c,d) Comparison of signal responses to pure toluene and the responses after humidity change subtraction. Gray, pure toluene; red dashed lines, $\Delta C_w = 20\%$RH; blue dashed lines, $\Delta C_w = -20\%$RH. See also Fig. S11 in the Supplemental Material [34] for comparison between the pure signal and subtracted responses.

xylenes), which are widely recognized as common toxic gases due to their carcinogenicity, neurotoxicity, and ubiquitous emission contributions to environmental pollution [35]. BTEX are also known for their similar chemical properties and limited solubility in water, allowing for the assumption of independent sorption behavior for each component. This independence facilitated the extraction of sorption kinetic parameters and viscoelastic properties from the responses to single analyte systems. The MSS signal output was observed to follow the relationship $V_{\text{out}}(t) = \gamma\sigma(t) + V_0$, where γ represents a proportionality factor and V_0 denotes the baseline output. The measured responses highlighted the strong correlation between MSS signals and internal strain, consistent with previous findings in cantilever-type sensors [31, 32, 36].

Since the responses of three to four injection-purge cycles yielded more reliable parameter extractions compared to a single injection [28], we measured signal responses of PCL-coated MSS to pure water over four injection-purge cycles as shown in Fig. 4(a) and Fig. S4 in the Supplemental Material [34]. As mentioned in Fig. 2(a), the initial humidity C_w only affected the baseline as shown in Fig. 4(a) and Fig. S4 in the Supplemental Material [34]. Increasing the initial humidity from 0%RH to 40%RH increases the baseline (i.e., baseline $V_0 + \gamma\sigma_w$) from –10.871 ± 0.003 mV to –10.468 ± 0.002 and –10.095 ± 0.003 mV for 20%RH and 40%RH, respectively [Fig. 4(a)]. This corresponds to $\gamma\sigma_w$ = 0.40 [mV] for 20%RH and $\gamma\sigma_w$ = 0.78 [mV] for 40%RH. The responses to each pure BTEX with varied analyte concentrations were also measured (see also Fig. S4 in the Supplemental Material [34]). The sorption kinetic parameters of pure water ($\gamma\Delta\sigma_w$ and τ_w) and pure BETX ($\gamma\sigma_i$ and τ_s) as well as the viscoelastic parameters (τ_r and M_0/M_∞) were extracted as listed in Tables I and II. It was found that the sorption kinetic parameters ($\gamma\sigma_i$, τ_s, $\gamma\Delta\sigma_w$, and τ_w) vary depending on the chemical properties of individual analytes or water. In contrast, although the viscoelastic parameters (τ_r and M_0/M_∞) also vary to some extent possibly because of their different mechanical behaviors based on their chemical propoerties, the variation of them remained relatively small across different species, especially among BTEX.

It should be noted that the amplitude (intensity) to water $\gamma\Delta\sigma_w$ extracted from the signals to pure water are consistent with the baseline shifts $\gamma\sigma_w$. $\gamma\Delta\sigma_w$ for ΔC_w = 20%RH, 30%RH, and 40%RH are 0.41, 0.65, and 0.85 mV, respectively [Table I], while $\gamma\sigma_w$ observed in the baseline shifts for C_w = 20%RH and 40%RH are 0.40 and 0.78 mV, respectively, as noted above. The concentration-dependent sorption-induced strain ε_f in Eq. (2) is estimated by finite element analysis (FEA) through COMSOL multiphysics according to the literatures [37, 38]. The p-type piezoresistors embedded in the sensing beams of MSS are created by boron diffusion onto a single-crystal silicon with a (100) surface [31]. Assuming plain stress (i.e., $\sigma_z = 0$), each relative resistance change can be approximated as [31, 32]

$$\frac{\Delta R}{R} \approx \frac{1}{2}\pi_{44}\left(\sigma_x - \sigma_y\right), \tag{16}$$

where π_{44} is one of the fundamental piezoresistance coefficients of the silicon crystal; σ_x, σ_y, and σ_z are stresses induced on the piezoresistor in [111], [1$\bar{1}$0], and [001] directions of the crystal, respectively [Fig. 1(b)] [32]. The signal output of MSS V_{out} is provided by the total output resistance change obtained from the Wheatstone bridge circuit and given by [31, 32]

$$V_{\text{out}} = \frac{V_B}{4}\left(\frac{\Delta R_1}{R_1} - \frac{\Delta R_2}{R_2} + \frac{\Delta R_3}{R_3} - \frac{\Delta R_4}{R_4}\right), \tag{17}$$

where V_B is the bridge voltage applied to the Wheatstone bridge circuit (i.e., $V_B = -0.5$ [V] in this study) and $\Delta R_i/R_i$ are the relative resistance changes in each sensing beam [Fig. 1(b)]. Using representative values for M_∞ and Poisson's ratio of PCL [39, 40], total relative resistance change $\Delta R/R|_{\text{total}}$ per stain is estimated as 1.13 by FEA. From Eq. (17), this corresponds to 1.52×10^{-4} strain per %RH. These results confirm the validity of the present model for humidity effects as sorption-induced strain corresponding to the initial humidity C_w and the humidity difference ΔC_w.

Using the derived equation in Eq. (9) with extracted parameters obtained from pure water and pure BTEX [Tables I and II], we further verified the model for predicting the signal responses to BTEX under varied humidity conditions. The observed baseline shifts in Figs. 4(b)–4(d) correspond to

the initial humidity ranging from 0%RH to 40%RH. These baseline shifts are consistent with those observed in the responses to pure water [Fig. 4(a)]. Meanwhile, the changes in the initial humidity have no significant influence on the signal responses, which aligns with the numerical results presented in Fig. 2(a). Figure 4(e)–4(h) show the responses to each BTEX under varied humidity differences ΔC_w (see also for the different initial humidity C_w in Fig. S5 in the Supplemental Material [34]). By applying the theoretical concentration profiles controlled by MFCs to calculate each response to humidified analyte mixtures, the predicted responses using Eq. (9) were compared with experimental data in Figs. 4(b)–4(l) (see also Figs. S5–S7 in the Supplemental Material [34]). The predicted responses agree well with the experimentally measured responses to BTEX with concentrations C_g varied at 5%, 10%, and 15% under varied humidity differences ΔC_w at 20%RH, 30%RH, and 40%RH, demonstrating the potential of the present model in capturing complex interactions under humid environments.

We also demonstrated the cases of negative humidity changes, as discussed in Fig. 2(b). Figures 5(a) and 5(b) show the dynamic responses of PCL-coated MSS to 5% toluene vapor with both positive and negative humidity changes ($\Delta C_w = \pm$20%RH) under different initial humidity conditions ($C_w =$ 20%RH and 40%RH). Using Eq. (9) along with the extracted parameters obtained from pure water and pure toluene [Tables I and II], the signal responses were predicted. Although the humidity influence on the responses to toluene vapors is small because of the lower sensitivity of PCL-coated MSS to water compared to toluene, the predicted responses show good agreement with the experimentally measured signal responses as shown in Figs. 5(a) and 5(b) (see also Figs. S8–S10 in the Supplemental Material [34]). These results indicate the potential of the present model for predicting the signal responses under various humidity conditions.

Since we achieved the prediction of signal responses under various humidity conditions, the present model suggests the possibility of subtracting the humidity influences. To demonstrate this in practical terms, we subtracted humidity influences using the humidity responses predicted by Eq. (9) from the responses under the positive and negative humidity differences. The subtracted responses showed excellent overlap with the responses to pure toluene vapor, as shown in Figs. 5(c) and 5(d). Additional details regarding the subtraction for other analyte concentrations are provided in Figs. S8–S11 in the Supplemental Material [34]. The results support that the pure analyte signals in humidified samples can be accurately extracted, enabling reliable quantification of analyte concentrations.

VI. CONCLUSION

We propose an analytical model for humidity effects in nanomechanical sensing based on sorption kinetics and viscoelastic behaviors of receptor materials. By this analytical model, the humidity influences observed in previous studies [9, 11] were theoretically revealed, i.e., the existence of features robust to the effects of humidity [9] and the robust extraction of the diffusion time constant τ_s under varying initial humidity [11]. The model was experimentally validated using BTEX as target analytes on MSS under various humidity conditions, demonstrating excellent agreement between theoretical predictions and output responses. It should be noted that the present model can be applicable in the practical cases of olfactory sensors by subtracting the humidity influences. This capability enables the elimination of humidity interference, isolating the analyte-specific sensing signals. Since the present model can be extended to multi-component analytes [29], the proposed model provides a robust approach to analyzing analytes in various humid environments, offering significant potential for applications of nanomechanical sensors as olfactory sensors in odor detection, environmental monitoring, and healthcare and medical diagnosis.

ACKNOWLEDGEMENTS

M.-Q.F. and Y.Z. thanks NIMS Junior program, NIMS. K.M. acknowledges the International Center for Young Scientists (ICYS) program, NIMS, Japan. Y.Z. thanks the Support by Pioneering Research Initiated by the Next Generation (SPRING) program, JST, MEXT, Japan.

This study was financially supported by a Grant-in-Aid for Scientific Research (A), JSPS, MEXT, Japan (no. 18H04168); a Grant-in-Aid for Scientific Research (C), JSPS, MEXT, Japan (no. 22K05324); a Grant-in-Aid for Challenging Research (Pioneering), JSPS, MEXT, Japan (no. 20K20554); the Public/Private R&D Investment Strategic Expansion Program (PRISM), Cabinet Office, Japan; the Support by Pioneering Research Initiated by the Next Generation (SPRING), JST, MEXT, Japan (no. JPMJSP2124); and ICYS, NIMS.

DATA AVAILABILITY

The data are not publicly available. The data are available from the authors upon reasonable request.

Appendix A: Recurrence relations of the dynamic stress change

The substitution of Eqs. (2) and (7) into Eq. (1) yields the differential equation of the dynamic stress change in a viscoelastic receptor of nanomechanical sensors at the n-th step $\sigma_n(t)$. Although Eq. (3) is a step function, the dynamic stress change must be a continuous function. As for the boundary conditions at $t = t_n$, the stress $\sigma_n(t_n)$ should be equal to $\sigma_{n+1}(t_n)$ and the stress at the beginning of the first injection ($t = t_0$) can be assumed as zero, i.e., $\sigma_{n=1}(t_0) = 0$. The differential equation can be solved and found the recurrence relation between the $2m$-th and $2(m+1)$-th purge processes and that between $(2m+1)$-th injection and $2m$-th purge processes as

$$\sigma_{2m+1}(t)-\sigma_{2m}(t)=\sigma_i\alpha_i\left(1-e^{-\frac{t-t_{2m}}{\tau_s}}\right)+\Delta\sigma_w\alpha_w\left(1-e^{-\frac{t-t_{2m}}{\tau_w}}\right)+\left[\sigma_i(1-\alpha_i)+\Delta\sigma_w(1-\alpha_w)\right]\left(1-e^{-\frac{t-t_{2m}}{\tau_r}}\right), \tag{A1a}$$

$$\begin{aligned}\sigma_{2(m+1)}(t)-\sigma_{2m}(t)=&\sigma_i\alpha_i\left(e^{-\frac{t-t_{2m+1}}{\tau_s}}-e^{-\frac{t-t_{2m}}{\tau_s}}\right)+\Delta\sigma_w\alpha_w\left(e^{-\frac{t-t_{2m+1}}{\tau_w}}-e^{-\frac{t-t_{2m}}{\tau_w}}\right)\\&+\left[\sigma_i(1-\alpha_i)+\Delta\sigma_w(1-\alpha_w)\right]\left(e^{-\frac{t-t_{2m+1}}{\tau_r}}-e^{-\frac{t-t_{2m}}{\tau_r}}\right),\end{aligned} \tag{A1b}$$

with the stresses at the first injection and purge processes given by

$$\sigma_{n=1}(t)=\sigma_w+\sigma_i\left(1-\alpha_i e^{-\frac{t-t_0}{\tau_s}}\right)+\Delta\sigma_w\left(1-\alpha_w e^{-\frac{t-t_0}{\tau_w}}\right)-\left[\sigma_i(1-\alpha_i)+\Delta\sigma_w(1-\alpha_w)\right]e^{-\frac{t-t_0}{\tau_r}}, \tag{A2a}$$

$$\sigma_{n=2}(t)=\sigma_w+\sigma_i\alpha_i\left(e^{-\frac{t-t_1}{\tau_s}}-e^{-\frac{t-t_0}{\tau_s}}\right)+\Delta\sigma_w\alpha_w\left(e^{-\frac{t-t_1}{\tau_w}}-e^{-\frac{t-t_0}{\tau_w}}\right)+\left[\sigma_i(1-\alpha_i)+\Delta\sigma_w(1-\alpha_w)\right]\left(e^{-\frac{t-t_1}{\tau_r}}-e^{-\frac{t-t_0}{\tau_r}}\right), \tag{A2b}$$

for the case of $\tau_s\neq\tau_r\neq\tau_w$,

$$\sigma_{2m+1}(t)-\sigma_{2m}(t)=\sigma_i\left(1-e^{-\frac{t-t_{2m}}{\tau_r}}\right)+\Delta\sigma_w\left(1-\alpha_w e^{\frac{t-t_{2m}}{\tau_w}}\right)+\sigma_i\beta_r(t-t_{2m})e^{-\frac{t-t_{2m}}{\tau_r}}-\Delta\sigma_w(1-\alpha_w)e^{-\frac{t-t_{2m}}{\tau_r}}, \tag{A3a}$$

$$\begin{aligned}\sigma_{2(m+1)}(t)-\sigma_{2m}(t)=&\left[\sigma_i+\Delta\sigma_w(1-\alpha_w)\right]\left(e^{-\frac{t-t_{2m+1}}{\tau_r}}-e^{-\frac{t-t_{2m}}{\tau_r}}\right)+\Delta\sigma_w\alpha_w\left(e^{-\frac{t-t_{2m+1}}{\tau_w}}-e^{-\frac{t-t_{2m}}{\tau_w}}\right)\\&-\sigma_i\beta_r\left[(t-t_{2m+1})e^{-\frac{t-t_{2m+1}}{\tau_r}}-(t-t_{2m})e^{-\frac{t-t_{2m}}{\tau_r}}\right],\end{aligned} \tag{A3b}$$

with the stresses at the first injection and purge processes given by

$$\sigma_{n=1}(t)=\sigma_w+\sigma_i\left(1-e^{-\frac{t-t_0}{\tau_r}}\right)+\Delta\sigma_w\left(1-\alpha_w e^{-\frac{t-t_0}{\tau_w}}\right)+\sigma_i\beta_r(t-t_0)e^{-\frac{t-t_0}{\tau_r}}-\Delta\sigma_w(1-\alpha_w)e^{-\frac{t-t_0}{\tau_r}}, \tag{A4a}$$

$$\begin{aligned}\sigma_{n=2}(t)=&\sigma_w+\left[\sigma_i+\Delta\sigma_w(1-\alpha_w)\right]\left(e^{-\frac{t-t_1}{\tau_r}}-e^{-\frac{t-t_0}{\tau_r}}\right)+\Delta\sigma_w\alpha_w\left(e^{-\frac{t-t_1}{\tau_w}}-e^{-\frac{t-t_0}{\tau_w}}\right)\\&-\sigma_i\beta_r\left[(t-t_1)e^{-\frac{t-t_1}{\tau_r}}-(t-t_0)e^{-\frac{t-t_0}{\tau_r}}\right],\end{aligned} \tag{A4b}$$

for the case of $\tau_s=\tau_r\neq\tau_w$, and

$$\sigma_{2m+1}(t)-\sigma_{2m}(t)=\sigma_i\left(1-\alpha_i e^{-\frac{t-t_{2m}}{\tau_s}}\right)+\Delta\sigma_w\left(1-e^{\frac{t-t_{2m}}{\tau_r}}\right)+\Delta\sigma_w\beta_r(t-t_{2m})e^{-\frac{t-t_{2m}}{\tau_r}}-\sigma_i(1-\alpha_i)e^{-\frac{t-t_{2m}}{\tau_r}}, \tag{A5a}$$

$$\begin{aligned}\sigma_{2(m+1)}(t)-\sigma_{2m}(t)=&\left[\sigma_i(1-\alpha_i)+\Delta\sigma_w\right]\left(e^{-\frac{t-t_{2m+1}}{\tau_r}}-e^{-\frac{t-t_{2m}}{\tau_r}}\right)+\sigma_i\alpha_i\left(e^{-\frac{t-t_{2m+1}}{\tau_s}}-e^{-\frac{t-t_{2m}}{\tau_s}}\right)\\&-\Delta\sigma_w\beta_r\left[(t-t_{2m+1})e^{-\frac{t-t_{2m+1}}{\tau_r}}-(t-t_{2m})e^{-\frac{t-t_{2m}}{\tau_r}}\right],\end{aligned} \tag{A5b}$$

with the stresses at the first injection and purge processes given by

$$\sigma_{n=1}(t)=\sigma_w+\sigma_i\left(1-\alpha_i e^{-\frac{t-t_0}{\tau_s}}\right)+\Delta\sigma_w\left(1-e^{-\frac{t-t_0}{\tau_r}}\right)+\Delta\sigma_w\beta_r(t-t_0)e^{-\frac{t-t_0}{\tau_r}}-\sigma_i(1-\alpha_i)e^{-\frac{t-t_0}{\tau_r}}, \tag{A6a}$$

$$\begin{aligned}\sigma_{n=2}(t)=&\sigma_w+\left[\sigma_i(1-\alpha_i)+\Delta\sigma_w\right]\left(e^{-\frac{t-t_1}{\tau_r}}-e^{-\frac{t-t_0}{\tau_r}}\right)+\sigma_i\alpha_i\left(e^{-\frac{t-t_1}{\tau_s}}-e^{-\frac{t-t_0}{\tau_s}}\right)\\&-\Delta\sigma_w\beta_r\left[(t-t_1)e^{-\frac{t-t_1}{\tau_r}}-(t-t_0)e^{-\frac{t-t_0}{\tau_r}}\right],\end{aligned} \tag{A6b}$$

for the case of $\tau_s\neq\tau_r=\tau_w$, where α_i, α_w, and β_r are given in Eqs. (11) and (13).

[1] K. Minami, G. Imamura, R. Tamura, K. Shiba, and G. Yoshikawa, Recent advances in nanomechanical membrane-type surface stress sensors towards artificial olfaction, Biosen-

sors **12**, 762 (2022).
[2] K. Shiba, R. Tamura, G. Imamura, and G. Yoshikawa, Data-driven nanomechanical sensing: specific information extraction from a complex system, Sci. Rep. **7**, 3661 (2017).
[3] K. Shiba, R. Tamura, T. Sugiyama, Y. Kameyama, K. Koda, E. Sakon, K. Minami, H. T. Ngo, G. Imamura, K. Tsuda, and G. Yoshikawa, Functional nanoparticles-coated nanomechanical sensor arrays for machine learning-based quantitative odor analysis, ACS Sens. **3**, 1592 (2018).
[4] K. Shiba, G. Imamura, and G. Yoshikawa, Odor-based nanomechanical discrimination of fuel oils using a single type of designed nanoparticles with nonlinear viscoelasticity, ACS Omega **6**, 23389–23398 (2021).
[5] H. Xu, K. Kitai, K. Minami, M. Nakatsu, G. Yoshikawa, K. Tsuda, K. Shiba, and R. Tamura, Determination of quasi-primary odors by endpoint detection, Sci. Rep. **11**, 12070 (2021).
[6] K. Minami, M. Matoba, R. Nakakubo, and G. Yoshikawa, Detection of acetone in milk through odor towards monitoring of ketosis in dairy cows, in *2024 IEEE International Symposium on Olfaction and Electronic Nose (ISOEN)* (2024) pp. 1–4.
[7] F. Loizeau, H. P. Lang, T. Akiyama, S. Gautsch, P. Vettiger, A. Tonin, G. Yoshikawa, C. Gerber, and N. de Rooij, Piezoresistive membrane-type surface stress sensor arranged in arrays for cancer diagnosis through breath analysis, in *2013 IEEE 26th International Conference on Micro Electro Mechanical Systems (MEMS)* (2013) pp. 621–624.
[8] H. P. Lang, F. Loizeau, A. Hiou-Feige, J. P. Rivals, P. Romero, T. Akiyama, C. Gerber, and E. Meyer, Piezoresistive membrane surface stress sensors for characterization of breath samples of head and neck cancer patients, Sensors **16**, 1149 (2016).
[9] K. Inada, H. Kojima, Y. Cho-Isoda, R. Tamura, G. Imamura, K. Minami, T. Nemoto, and G. Yoshikawa, Statistical evaluation of total expiratory breath samples collected throughout a year: Reproducibility and applicability toward olfactory sensor-based breath diagnostics, Sensors **21**, 4742 (2021).
[10] Y. Saeki, N. Maki, T. Nemoto, K. Inada, K. Minami, R. Tamura, G. Imamura, Y. Cho-Isoda, S. Kitazawa, H. Kojima, G. Yoshikawa, and Y. Sato, Lung cancer detection in perioperative patients' exhaled breath with nanomechanical sensor array, Lung Cancer (2024).
[11] K. Minami, Y. Zhou, G. Imamura, K. Shiba, and G. Yoshikawa, Sorption kinetic parameters from nanomechanical sensing for discrimination of 2-nonenal from saturated aldehydes., ACS Sens. **9**, 689 (2024).
[12] J. K. Hart and K. Martinez, Environmental sensor networks: A revolution in the earth system science?, Earth-Sci. Rev. **78**, 177 (2006).
[13] C. K. Ho, A. Robinson, D. R. Miller, and M. J. Davis, Overview of sensors and needs for environmental monitoring, Sensors **5**, 4 (2005).
[14] A. D. Wilson and M. Baietto, Applications and advances in electronic-nose technologies, Sensors **9**, 5099 (2009).
[15] H. Tai, S. Wang, Z. Duan, and Y. Jiang, Evolution of breath analysis based on humidity and gas sensors: Potential and challenges, Sens. Actuators B: Chem. **318**, 128104 (2020).
[16] E. T. Zellers and M. Han, Effects of temperature and humidity on the performance of polymer-coated surface acoustic wave vapor sensor arrays, Anal. Chem. **68**, 2409 (1996).
[17] Z. Zhao, M. Knight, S. Kumar, E. T. Eisenbraun, and M. A. Carpenter, Humidity effects on Pd/Au-based all-optical hydrogen sensors, Sens. Actuators B: Chem. **129**, 726 (2008).
[18] P. Wei, Z. Ning, S. Ye, L. Sun, F. Yang, K. C. Wong, D. Westerdahl, and P. K. K. Louie, Impact analysis of temperature and humidity conditions on electrochemical sensor response in ambient air quality monitoring, Sensors **18**, 59 (2018).
[19] R. Huerta, T. Mosqueiro, J. Fonollosa, N. F. Rulkov, and I. Rodriguez-Lujan, Online decorrelation of humidity and temperature in chemical sensors for continuous monitoring, Chemom. Intell. Lab. Syst. **157**, 169 (2016).
[20] J. K. Gimzewski, C. Gerber, E. Meyer, and R. R. Schlittler, Observation of a chemical-reaction using a micromechanical sensor, Chem. Phys. Lett. **217**, 589 (1994).
[21] J. E. Sader, Surface stress induced deflections of cantilever plates with applications to the atomic force microscope: Rectangular plates, J. Appl. Phys. **89**, 2911 (2001).
[22] R. B. Karabalin, L. G. Villanueva, M. H. Matheny, J. E. Sader, and M. L. Roukes, Stress-induced variations in the stiffness of micro- and nanocantilever beams, Phys. Rev. Lett. **108**, 236101 (2012).
[23] G. Yoshikawa, Mechanical analysis and optimization of a microcantilever sensor coated with a solid receptor film, Appl. Phys. Lett. **98**, 173502 (2011).
[24] Z. Y. Hu, T. Thundat, and R. J. Warmack, Investigation of adsorption and absorption-induced stresses using microcantilever sensors, J. Appl. Phys. **90**, 427 (2001).
[25] S. M. Heinrich, M. J. Wenzel, F. Josse, and I. Dufour, An analytical model for transient deformation of viscoelastically coated beams: Applications to static-mode microcantilever chemical sensors., J. Appl. Phys. **105**, 124903 (2009).
[26] M. J. Wenzel, F. Josse, S. M. Heinrich, E. Yaz, and P. G. Datskos, Sorption-induced static bending of microcantilevers coated with viscoelastic material, J. Appl. Phys. **103**, 064913 (2008).
[27] M. J. Wenzel, F. Josse, and S. M. Heinrich, Deflection of a viscoelastic cantilever under a uniform surface stress: Applications to static- mode microcantilever sensors undergoing adsorption, J. Appl. Phys. **105**, 064903 (2009).
[28] K. Minami, K. Shiba, and G. Yoshikawa, Sorption-induced static mode nanomechanical sensing with viscoelastic receptor layers for multistep injection-purge cycles, J. Appl. Phys. **129**, 124503 (2021).
[29] K. Minami and G. Yoshikawa, An analytical model of sorption-induced static mode nanomechanical sensing for multi-component analytes, arXiv , arXiv:2501.03597 (2025).
[30] T. Yakabe, G. Imamura, G. Yoshikawa, N. Miyauchi, M. Kitajima, and A. N. Itakura, 2-step reaction kinetics for hydrogen absorption into bulk material via dissociative adsorption on the surface, Sci. Rep. **11**, 18836 (2021).
[31] G. Yoshikawa, T. Akiyama, S. Gautsch, P. Vettiger, and H. Rohrer, Nanomechanical membrane-type surface stress sensor, Nano Lett. **11**, 1044 (2011).
[32] G. Yoshikawa, T. Akiyama, F. Loizeau, K. Shiba, S. Gautsch, T. Nakayama, P. Vettiger, N. F. de Rooij, and M. Aono, Two dimensional array of piezoresistive nanomechanical membrane-type surface stress sensor (MSS) with improved sensitivity, Sensors **12**, 15873 (2012).
[33] W. Flügge, *Viscoelasticity*, 2nd ed. (Springer, New York, 1975).
[34] See Supplemental Material at [URL: http://...] for detailed numerical calculations and supporting figures.
[35] B. Yu, Z. Yuan, and F. Yu, Z.; Xue-song, BTEX in the environment: An update on sources, fate, distribution, pretreatment, analysis, and removal techniques, Chem. Eng. J. **435**, 134825 (2022).
[36] F. Loizeau, T. Akiyama, S. Gautsch, P. Vettiger, G. Yoshikawa, and N. F. de Rooij, Comparing membrane- and cantilever-based surface stress sensors for reproducibility, Sens. Actuators A: Phys. **228**, 9 (2015).

[37] H. H. M. Yeung, G. Yoshikawa, K. Minami, and K. Shiba, Strain-based chemical sensing using metal–organic framework nanoparticles, J. Mater. Chem. A **8**, 18007 (2020).

[38] K. Minami and G. Yoshikawa, Finite element analysis of interface dependence on nanomechanical sensing, Sensors **5**, 1518 (2020).

[39] S. Eshraghi and S. Das, Mechanical and microstructural properties of polycaprolactone scaffolds with one-dimensional, two-dimensional, and three-dimensional orthogonally oriented porous architectures produced by selective laser sintering, Acta Biomater. **6**, 2467 (2010).

[40] H. Doyle, S. Lohfeld, and P. McHugh, Predicting the elastic properties of selective laser sintered pcl/-tcp bone scaffold materials using computational modelling, Ann. Biomed. Eng. **42**, 661 (2014).